

The catalog of variable sources detected by *INTEGRAL* I: Catalog and techniques [★]

I. Telezhinsky^{1,2}, D. Eckert^{3,4,5}, V. Savchenko^{4,5}, A. Neronov^{4,5}, N. Produit^{4,5}, and T.J.-L. Courvoisier^{4,5}

¹ DESY Zeuthen, Platanenallee 6, 15738 Zeuthen, Germany

² Astronomical Observatory of Kiev University, Observatorna 3, 04058 Kiev, Ukraine

³ INAF/IASF Milano, Via E. Bassini 15, 20133 Milano, Italy

⁴ ISDC Data Centre for Astrophysics, Chemin d'Ecogia 16, CH-1290 Versoix, Switzerland

⁵ Observatoire Astronomique de l'Université de Genève, Chemin des Maillettes 51, CH-1290 Sauverny, Switzerland

Received / Accepted

ABSTRACT

Context. During its 6 years of operation, *INTEGRAL*/ISGRI has detected more than 500 sources. Many of these sources are variable. Taking into account that nearly half of *INTEGRAL*/ISGRI sources are new and many of them remain unidentified, the variability properties of the sources can provide additional constraints to help us to classify and identify the unknown sources.

Aims. To study the variability properties of the sources detected by *INTEGRAL*/ISGRI, we develop a method to quantify the variability of a source. We describe here our techniques and compile a catalog of the sources that fit our criteria of variability.

Methods. We use the natural time binning of *INTEGRAL* observations called Science Window (≈ 2000 seconds) and test the hypothesis that the detected sources are constant using a χ^2 all-sky map in three energy bands (20-40, 40-100, 100-200 keV). We calculate an intrinsic variance of the flux in individual pixels and use it to define the fractional variability of a source. The method is sensitive to the source variability on timescales of one Science Window and higher. We concentrate only on the sources that were already reported to be detected by *INTEGRAL*.

Results. We present a catalog of 202 sources found to be significantly variable. For the catalog sources, we give the measure of variability and fluxes with corresponding errors in the 20-40, 40-100 and 100-200 keV energy bands, and we present some statistics about the population of variable sources. The description of the physical properties of the variable sources will be given in a forthcoming paper.

Key words. Gamma-rays: observations, catalogs

1. Introduction

INTEGRAL (INTErnational Gamma Ray Astrophysics Laboratory, Winkler et al. (2003)) was launched in 2002 and since then has performed high-quality observations in the energy band from 3 keV up to ~ 10 MeV. The *INTEGRAL* payload consists of two main soft gamma-ray instruments (the imager IBIS (Ubertini et al. 2003), and the spectrometer SPI (Vedrenne et al. 2003)) and two monitors (in X-rays JEM-X (Lund et al. 2003), and in optical OMC (Mas-Hesse et al. 2003)). The wide field-of-view of the imager IBIS provides an ideal opportunity to survey the sky in hard X-rays.

During its first 6 years in orbit, *INTEGRAL* has covered nearly the whole sky. The observational data have been mainly used to study the soft gamma-ray emission from the Galactic plane (GP) (Bouchet et al. 2005; Krivonos et al. 2007) through the Galactic plane scans and the Galactic centre (GC) Bélanger et al. (2004); Revnivtsev et al. (2004); Bélanger et al. (2006); Krivonos et al. (2007) through the Galactic centre deep exposure programme. A number of papers have already presented general surveys (Bazzano et al. 2006; Bird et al. 2007) of the sky as well as of specific regions (Götz et al. 2006;

den Hartog et al. 2006; Molkov et al. 2004) and population types (Barlow et al. 2006; Bassani et al. 2007; Sazonov et al. 2007; Beckmann et al. 2006, 2009).

The majority of the classified sources detected by *INTEGRAL* are either low and high mass X-ray binaries (LMXBs and HMXBs) or AGNs (Bodaghee et al. 2007). However, a significant fraction of the detected sources remain unidentified. A special approach to population classification is required for the GC region to resolve the population types because of the high density of sources. Fortunately, the physics of the sources may help us to unveil their type. Indeed, the bulk of the *INTEGRAL* sources are accreting systems that are expected to be intrinsically variable on multiple timescales depending on the source type and the nature of the variability. For instance, X-ray binaries (XRBs) may exhibit variability on timescales that range from milliseconds (supporting the idea that emission originates close to the compact object in the inner accretion radius) to hours and days, indicating that the variability can originate throughout the accretion flow at multiple radii and propagate inwards to modulate the central X-ray emission (Arévalo & Uttley 2006). This idea is supported by the known correlation between millisecond/second and hour/day scale variability in XRBs (Uttley 2004). LMXBs may exhibit flaring behavior with an increase in both emission intensity and hardness over a period of a few hundred to a few thousand seconds. X-ray bursts with rise times of a few seconds

Send offprint requests to: telezhinsky@gmail.com

* Table 3 is also available in electronic form at the CDS via anonymous ftp to cdsarc.u-strasbg.fr (130.79.128.5) or via <http://cdsarc.u-strasbg.fr/viz-bin/qcat?J/A+A/vol/page>

and decay times of hundreds of seconds or even several hours (Barnard et al. 2002) are also common to these objects. On the other hand, HMXBs are known to exhibit variability on timescales ranging from a fraction of a day up to several days, generated by the clumpiness of the stellar wind accreting onto the compact object (Ducci et al. 2009). Hour-long outbursts caused by variable accretion rates are observed in supergiant fast X-ray transients, a sub-class of HMXBs discovered by *INTEGRAL* (Romano et al. 2009). Owing to their larger size, AGNs of different types exhibit day-to-month(s) variability depending on the black hole mass (Ishibashi & Courvoisier 2009). Gamma-ray loud blazars have variability timescales in the range from $10^{1.6}$ to $10^{5.6}$ s (Liang & Liu 2003). Therefore, a list of *INTEGRAL* sources with quantitative measurements of their variability would be an important help to classifying the unidentified sources and more detailed studies of their physics.

The variability of *INTEGRAL* sources was addressed in the latest 4th IBIS/ISGRI survey catalog paper (Bird et al. 2010) when the authors performed the so-called *bursticity* analysis intended to facilitate the detection of variable sources.

Here we present a catalog of *INTEGRAL* variable sources identified in a large fraction of the archival public data. In addition to standard maps produced by the standard data analysis software, we compiled a χ^2 all-sky map and applied the newly developed method to measure the fractional variability of the sources detected by the IBIS/ISGRI instrument onboard *INTEGRAL*. The method is sensitive to variability on timescales longer than those of single ScW exposures (≈ 2000 seconds), i.e., to variability on timescales of hour(s)-day(s)-month(s). The catalog is compiled from the sources detected in the variability map. In addition, we implemented an online service providing the community with all-sky maps in the 20-40, 40-100, and 100-200 keV energy bands generated during the course of this research.

In the following, we describe the data selection procedure and the implemented data analysis pipeline (Sect. 2). In Sect. 3, we outline our systematic approach to the detection of variability in *INTEGRAL* sources and describe our detection procedure in Sect. 4. We compile the variability catalog in Sect. 5. In Sect. 6, we briefly describe the implemented all-sky map online service. We make some concluding remarks in Sect. 7.

2. Data and analysis

2.1. Data selection and filtering

Since its launch, *INTEGRAL* has performed over 800 revolutions each lasting for three days. We utilized the ISDC Data Centre for Astrophysics (Courvoisier et al. 2003) archive¹ to obtain all public data available up to June 2009 and the Offline Scientific Analysis (OSA) v. 7.0 to process the data.

INTEGRAL data are organized into science windows (ScWs), each being an individual observation that can be either of pointing or slew type. Each observation (pointing type) lasts 1 – 3 ksecs. For our analysis, we chose all pointing ScWs with an exposure time of at least 1 ksec. We filtered out revolutions up to and including 0025 belonging to the early performance verification phase, observations taken in staring mode,

and ScWs marked as bad time intervals in instrument characteristics data including ScWs taken during solar flares and radiation belt passages. Finally, after the reconstruction of sky images we applied the following statistical filtering. We calculated the standard deviation of the pixel distribution for each ScW and found the mean value of standard deviations for the whole data set. We then rejected all the ScWs in which the standard deviation exceeded the mean for the whole data set by more than 3σ . We assumed the distribution of standard deviations of individual and independent ScWs to be normal. While calculating standard deviations in individual ScWs, image pixels were assumed to be independent. Thus, the filtering procedure allowed us to remove all ScWs affected by a high background level. In the end, 43 724 unique pointing-type ScWs were selected for the analysis, giving us a total exposure time of 80.0 Msec and a more than 95 percent sky coverage.

2.2. Instrument and background

In the present study we use only the low-energy detector layer of the IBIS coded-mask instrument, called ISGRI (*INTEGRAL* Soft Gamma Ray Imager, Lebrun et al. (2003)), which consists of 16 384 independent CdTe pixels. It features an angular resolution of $12'$ (FWHM) and a source location accuracy of ~ 1 arcmin, depending on the signal significance (Gros et al. 2003). Its field of view (FOV) is $29^\circ \times 29^\circ$. The fully-coded part of the FOV (FCFOV), i.e., the area of the sky where the detector is fully illuminated by the hard X-ray sources, is $9^\circ \times 9^\circ$. It operates in the energy range between 15 keV and 1 MeV.

Over short timescales, the variability of the background of the instrument is assumed to be smaller than the statistical uncertainties. However, this is not the case for mosaic images constructed from long exposures. In general, it is assumed that the mean ISGRI background in each individual pixel changes very little with time, and therefore the standard OSA software provides only one background map for the entire mission. During the construction of the all-sky map, we noted that the quality of the mosaics of the extragalactic sky region depends on the time period over which the data were taken. We therefore, concluded that the long-term variation in the background of the instrument (Lebrun et al. 2005) significantly affects the extragalactic sky mosaic. On the other hand, in the GC and inner GP regions ($l\{-90; 90\}$, $b\{-20; 20\}$) the standard background maps provided by OSA provide better results (noise distributions are narrower). This might be because of the large number of bright sources and the Galactic ridge emission (Krivonos et al. 2007), although we leave this question open for the future research.

To produce time-dependent background maps, we extracted raw detector images for each *INTEGRAL* revolution (3 days) and calculated the mean count rate in each individual pixel during the corresponding time period. To remove the influence of the bright sources on the neighboring background, we fitted and removed these sources from the raw detector images, i.e., in each ScW we constructed a model of the source pattern on the detector (pixel illumination fraction, PIF) and fitted the raw detector images using the model

$$S_{k,l} = \sum_{i=1}^M f_i \times PIF_{k,l} + B, \quad (1)$$

where $S_{k,l}$ are the detector count rate, $PIF_{k,l}$ are the respective pattern model of source i in the detector pixel with coordinates

¹ <http://isdc.unige.ch>

(k, l) , f_i , $i = 1..M$ is the flux of source i in the given ScW, and B is the mean background level. This procedure was applied to all the detected sources in the FOV. The stability of the fitting procedure was tested using a large set ($> 1\,000$) of simulated ScWs with variable source fluxes. The results of the fit were normally distributed around the expected source flux, and therefore we can conclude that our procedure is sufficiently accurate to remove the point sources from the construction of the background maps. The results of the fitting procedure were then used to create a transformed detector image, $\hat{S}_{k,l}$, defined as

$$\hat{S}_{k,l} = S_{k,l} - \sum_{i=1}^M f_i \times PIF_{k,l}. \quad (2)$$

Background maps were then constructed by averaging the transformed detector images of a given data set.

From our time-dependent background maps, we found that the shape of the ISGRI background varies with time, in particular after each solar flare. A long-term change in the background was noticed as well. This result agrees with the findings of Lebrun et al. (2005). To take these variations into account, we generated background maps for each spacecraft revolution and in the image reconstruction step applied them to the extragalactic sky region.

Besides the real physical background of the sky, there is also artificial component, because IBIS/ISGRI is a coded-mask instrument with a periodic mask pattern. Therefore, the deconvolution of ISGRI images creates structures of fake sources that usually appear around bright sources. Apart from the periodicity of the mask, insufficient knowledge of the response function leads to residuals in the deconvolved sky images. The orientation of the spacecraft changes from one observation of the real source to another, so fake sources and structures around the real source contribute to the noise level of the local background. To reduce this contribution, we used a method described in Sect. 2.3.

2.3. Image reconstruction

After producing the background maps as described in the previous subsection, we started the analysis of the data using the standard Offline Scientific Analysis (OSA) package, version 7.0, distributed by ISDC (Courvoisier et al. 2003). For image reconstruction, we used a modified version of the method described in Eckert et al. (2008). It is known that screws and glue strips attaching the IBIS mask to the supporting structure can introduce systematic effects in the presence of very bright sources (Nevalainen et al. 2009). To remove these effects, we identified the mask areas where screws and glue absorb incoming photons, and we disregarded the pixels illuminated by these mask areas for the 11 brightest sources in the hard X-ray band. No more than 1% of the detector area was disregarded for each of the brightest sources. For weaker sources, the level of systematic errors produced by the standard OSA software was found to be consistent with the noise, so the modified method was not required. Finally, we summed all the processed images weighting by variances to create the all-sky mosaic. For this work, we produced mosaics in 3 energy bands (20-40, 40-100, and 100-200 keV). Both our all-sky map images and corresponding exposure maps are available online and we direct the reader to our online web service².

As an example, we provide here the image of the inner part (36° by 12°) of the Galaxy in the 20-40 keV energy band (see Fig. 2).

3. Method of variability detection

The variability of *INTEGRAL* sources can be analyzed in a standard way by studying the inconsistency of the detected signal with that expected from a constant source by performing the χ^2 test. Here we consider introducing a variability measurement for the *INTEGRAL* sources and show how to apply it to the specific case of the coded-mask instrument. For an alternative approach based on the maximum likelihood function for the determination of intrinsic variability of X-ray sources the reader is referred to Almaini et al. (2000) and Beckmann et al. (2007).

The *INTEGRAL* data are naturally organized by pointings (ScW) with average duration of $\sim 1 - 3$ ksec. Therefore, the simplest way to detect the variability of a source on ksec and longer timescales is to analyse the evolution of the flux from the source on a ScW-by-ScW basis. We define F_i and σ_i^2 to be the flux and the variance of a given source, respectively, in the i -th ScW. The weighted mean flux from the source is then given by

$$\langle F \rangle = \frac{\sum_{i=1}^N \frac{F_i}{\sigma_i^2}}{\sum_{i=1}^N \frac{1}{\sigma_i^2}}, \quad (3)$$

where N is the total number of ScWs. The variance of the source's flux, which is the mean squared deviation of the flux from its mean value during the observation time, is given by

$$S_{tot}^2 = \frac{\sum_{i=1}^N \frac{(F_i - \langle F \rangle)^2}{\sigma_i^2}}{\sum_{i=1}^N \frac{1}{\sigma_i^2}} = \chi^2 \sigma^2, \quad (4)$$

where $\chi^2 = \sum_{i=1}^N \frac{(F_i - \langle F \rangle)^2}{\sigma_i^2}$ and $\sigma^2 = \left(\sum_{i=1}^N \frac{1}{\sigma_i^2} \right)^{-1}$ is the variance of the weighted mean flux.

However, in addition to intrinsic variance of the source, this value includes the uncertainty in the flux measurements during individual ScWs, i.e., the contribution of the noise. If the source variance is caused only by the noise, i.e., $F_i = \langle F \rangle \pm \sigma_i$, Eq. (4) is given by $S_{noise}^2 = N\sigma^2$. To eliminate the noise contribution, we can subtract the noise term of the variance from the source variance and derive the *intrinsic variance* of the source

$$S_{int}^2 = \chi^2 \sigma^2 - N\sigma^2. \quad (5)$$

When all measurement errors are equal ($\sigma_i = \sigma_0$, $\sigma^2 = \sigma_0^2/N$), our case reduces to the method used by Nandra et al. (1997)

$$S_{int}^2 = \frac{1}{N} \sum_{i=1}^N (F_i - \bar{F})^2 - \sigma_0^2, \quad (6)$$

where \bar{F} is the unweighted mean flux and S_{int}^2 is called the *excess variance*. In the absence of measurement errors, our case reduces to the standard definition of the variance

$$S_{int}^2 = \frac{1}{N} \sum_{i=1}^N (F_i - \bar{F})^2. \quad (7)$$

Given that different sources have different fluxes, the variability of sources can be quantified by using the normalized measure of variability, which we call here the *fractional variability*

$$V = \frac{S_{int}}{\langle F \rangle}. \quad (8)$$

² <http://skyview.virgo.org.ua>

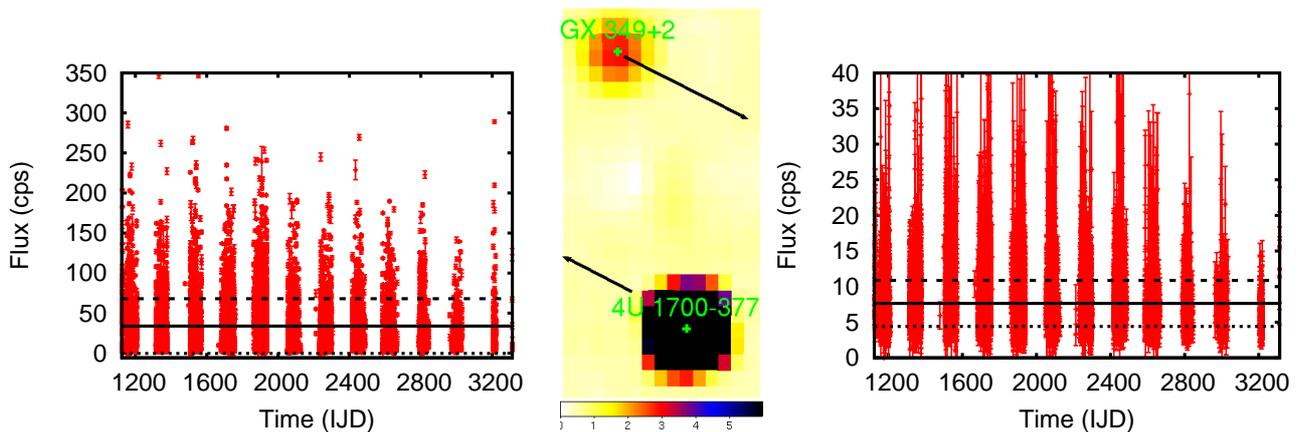


Fig. 1. Lightcurves and variability map of HMXB 4U 1700-377 and LMXB GX 349+2. The solid line indicates the mean flux of the sources during the observation time, the dotted line shows the mean flux minus S_{int} , the dashed line shows the mean flux plus S_{int} .

However, in reality, if one were to apply the above method to detect the variable sources in a crowded field (i.e., containing many sources) of a coded-mask instrument such as IBIS, one would infer *all* the detected sources to be highly variable. This is because in coded-mask instruments, each source casts a shadow of the mask on the detector plane. If there are several sources in the field of view, each of them produces a shadow that is spread over the whole detector plane. Some detector pixels are illuminated by more than one source. If the signal in a detector pixel is variable, one can tell, only with a certain probability, which of the sources illuminating this pixel is responsible for the variable signal. Thus, in a coded-mask instrument, the presence of bright variable sources in the field of view introduces an “artificial” variability for all the other sources illuminating the same pixels. Since the overlap between the PIF of the bright variable source and the sources at different positions on the sky varies with the position on the sky, one is also unable to determine in advance the level of this “artificial” variability in a given region of the deconvolved sky image.

To overcome this difficulty, one has to measure the variability of the flux not only directly in the sky pixels at the position of the source of interest, but also in the background pixels around the source. Obviously, the “artificial” variability introduced by the nearby bright sources is similar in the adjacent background pixels to that in the pixel(s) at the source position. Therefore, one can produce the variability map for the whole sky and compare the values of variability at the position of the source of interest to the mean values of variability in the adjacent background pixels. The variable sources should be visible as local excesses in the variability map of the region of interest. If a source can be localized in the variability image, then the true fractional variability of the source is calculated as

$$V_r = \frac{\sqrt{S_{int,s}^2 - S_{int,b}^2}}{\langle F_s \rangle - \langle F_b \rangle}, \quad (9)$$

where the subscript b represents the values of the background in the area adjacent to the source and the subscript s the values taken from the source position.

To illustrate the method, we present the lightcurves (Fig. 1) of two objects that are typical bright *INTEGRAL* sources: the HMXB 4U 1700-377, which is a very bright and very variable

source ($V_r \approx 104\%$), and the LMXB GX 349+2, which is a moderately bright and variable source ($V_r \approx 45\%$). The solid line indicates the mean flux of the sources, $\langle F \rangle$. We can see that the mean flux deviation (dotted lines), calculated as the square root of the intrinsic variance, S_{int}^2 , measures the average flux variation of the sources during the corresponding time. However, we note that in the present case we consider calculations based solely on a lightcurve. If one wishes to obtain a fractional variability value dividing the mean flux deviation by the mean flux, one will obtain the V value, but not V_r , i.e., the contribution of bright variable neighbor sources is not treated properly. It is impossible to extract the variability of the background, $S_{int,b}$, and the mean background flux $\langle F_b \rangle$ using the source lightcurve only. A number of lightcurves of the neighboring pixels should also be compiled to estimate $S_{int,b}$ and $\langle F_b \rangle$. This number should be sufficiently high to obtain good estimates. Therefore, an all-sky approach is justified. In the current example, no sources are much brighter in the vicinity of the ones considered that could strongly affect them, so the difference between V and the catalog V_r value is around 3%, but for the weak sources in the vicinity of bright ones the difference would be higher.

Looking at Eq. 9, one can indeed see that the effect of “artificial” fractional variability is strong for moderate and faint sources in the vicinity of the bright variable sources, while for bright sources the effect is small. The “artificial” variability introduced by the bright sources in their vicinity ($S_{int,b}^2$ for the surrounding sources) is in range from a fraction of a percent up to a few percent of their own variability (dictated by the PIF accuracy). When we consider the persistent source in the vicinity of the bright variable source, $S_{int,s}^2$ is defined by $S_{int,b}^2$ only (i.e., by variability introduced by the bright variable source). For moderate or faint sources, $S_{int,b}$ may well be comparable to their own flux, and if we apply Eq. 8 directly we will infer substantial fractional variability, which may well be between ten and fifty percent, or even higher. The bright sources are less sensitive to this effect because $S_{int,b}$ will be only a small fraction of their flux. We checked these conclusions by performing simulations of a moderate persistent source ($F = 1$ ct/s) in the vicinity of a bright variable source ($\langle F \rangle = 20$ ct/s). By applying Eq. 8 directly to measure the fractional variability of a moderate source, we found that $V \approx 25\%$ while Eq. 9 inferred that the source was constant, i.e., $V_r \approx 0\%$.

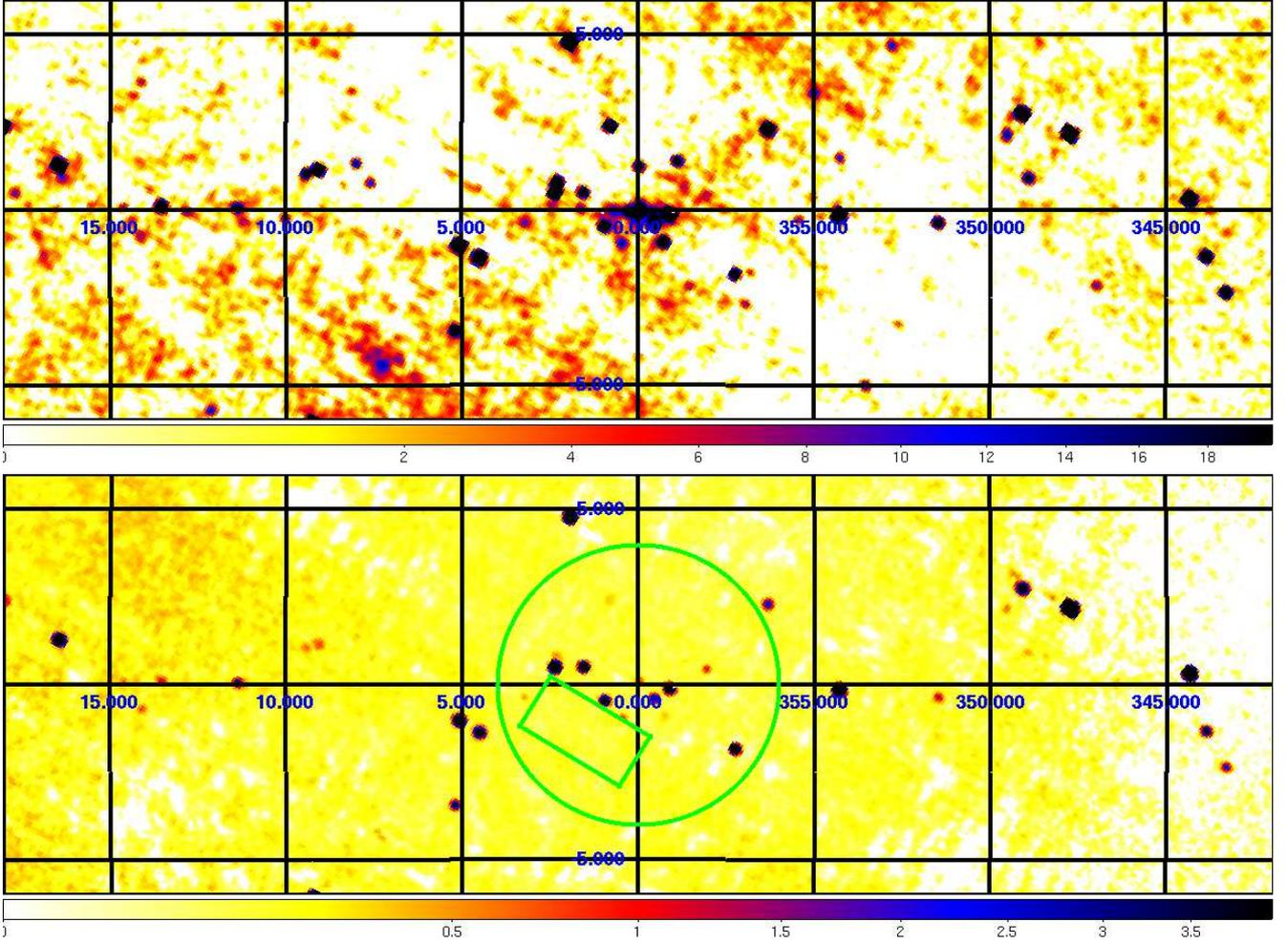


Fig. 2. Inner parts (36° by 12°) of the *INTEGRAL*/ISGRI all-sky maps in Galactic coordinates, Aitoff projection. The significance image (top) in the 20-40 keV energy band, has square root scaling. The bottom image shows the corresponding intrinsic variance map, and also has square root scaling. The circle shows the inner 4° for which the variability background extraction was made from the box region.

In the course of simulations, we also checked the behavior of the “artificial” variability in the case a moderate persistent source situated at the ghost position of the bright variable source. We considered two situations: a) when the mosaic image consisted mostly of ScWs in a configuration being determined almost entirely by the spacecraft orientation, which remained constant (i.e., sky region of the Crab), and b) when the mosaic image contained only a chance fraction of ScWs in that specific configuration because of different spacecraft orientations (i.e., sky region of the Cyg X-1). The simulations showed that the flux and therefore the variability measurement of the mosaic deviated from the input source parameters in case a) only, while in case b), there were no significant deviations. As expected in case a), the moderate source was affected. This was caused by the coincidence of the sources shadowgrams. The deconvolution procedure was unable to distinguish the sources correctly on the ScW level, therefore the mosaic results were affected. We detected an incorrect flux and variability for the moderate source. In reality, this particular simulated situation is very rare (see Sect. 5 for discussion of this situation in real case). Even if the constant orientation of some observation is kept, different observation patterns applied during the observation

will significantly reduce the undesirable effect considered in situation a).

4. The detection of variable sources

For our study, we used the latest distributed *INTEGRAL* reference catalog³ (Ebisawa et al. 2003) version 30 and selected the sources with ISGRI_FLAG == 1, i.e., all the sources ever detected by IBIS/ISGRI.

Based on the aforementioned method, we compiled the intrinsic variance maps (S_{int}^2) of the *INTEGRAL* sky in three energy bands (20-40, 40-100, and 100-200 keV). This was accomplished by performing pixel operations following Eq. (5) on the constructed all-sky mosaic maps of χ^2 , σ^2 (variance), and N , which is the map showing the number of ScWs used in a given pixel for the all-sky mosaic. As an example, the intrinsic variance image of the inner region of our Galaxy is given in Fig. 2 (see our online service for all-sky maps).

³ <http://isdc.unige.ch/?Data+catalogs>

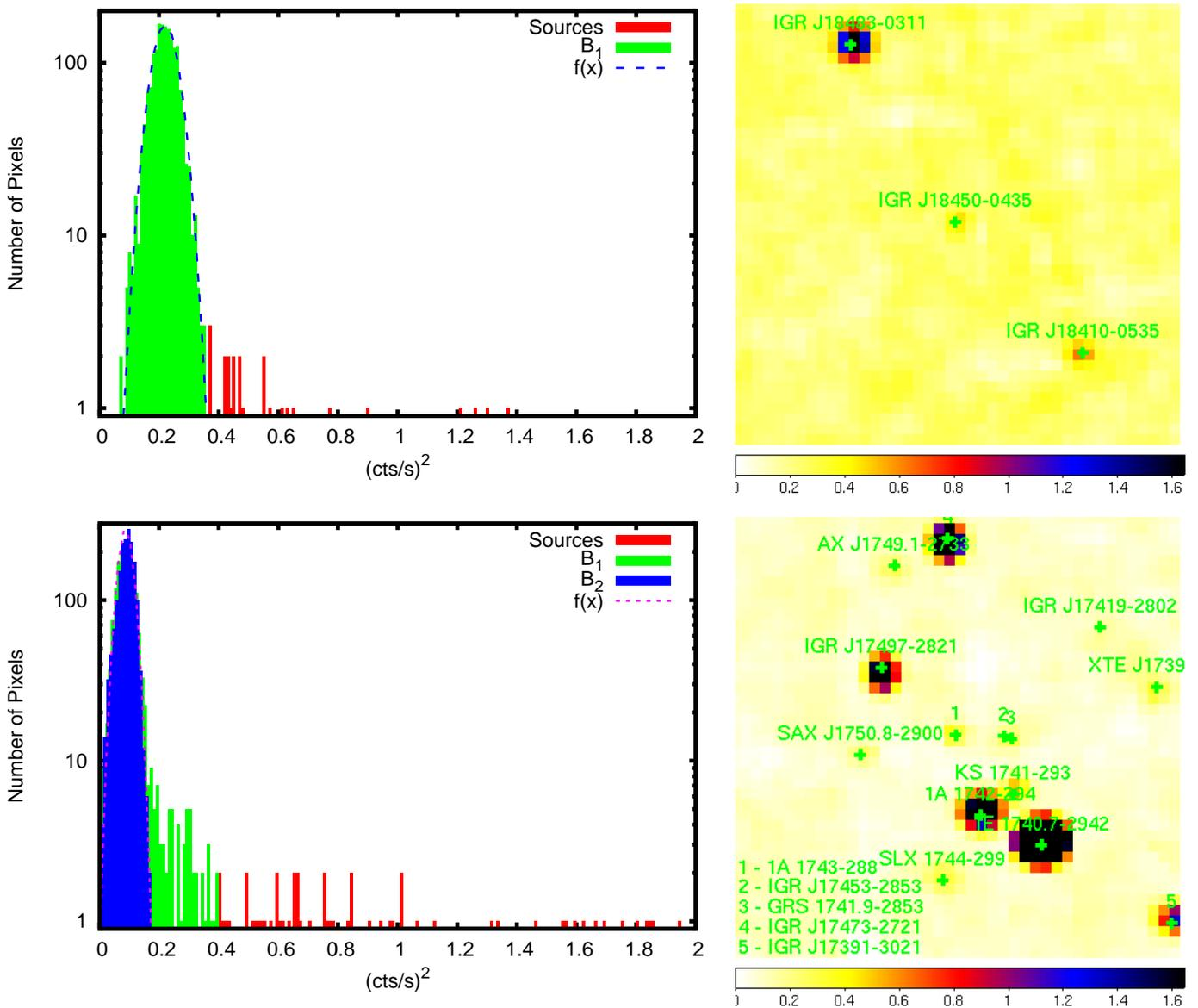


Fig. 3. Top: the distributions of the intrinsic variability in pixels of $3.5^\circ \times 3.5^\circ$ area (shown nearby) centered on the IGR J18450-0435. In green is B_1 distribution in the range $(min, 2m - min)$ here representing the local intrinsic variance background, in red is the sources contribution, $f(x)$ is the gaussian distribution. Bottom: the $3.5^\circ \times 3.5^\circ$ area (shown nearby) centered on the GC source 1A 1743-288. In green is B_1 distribution in the range $(min, 2m - min)$, in blue is B_2 distribution from the empty region in GC here representing the local intrinsic variance background, in red and $f(x)$ are same as above.

After compiling an intrinsic variance map in each band, we calculated the local (or background) intrinsic variance, $S_{int,b}^2$, and its scatter, Σ , in the region around each catalog source. This was performed by the following scheme. First, the values of the mean m , the minimum min , and their difference were calculated in a square of $3.5^\circ \times 3.5^\circ$ centered on the source position. We then assumed that the pixel values in the corresponding area are distributed normally and there is the always-positive contribution from the sources in the field. Since the sources occupy a small fraction of the considered sky region, the initial mean value, m , is almost unaffected by their presence because of their small contribution. To reject the source contribution and to obtain the parameters of the normal component, we calculated the mean and the standard deviation in the range $(min, 2m - min)$. The newly found mean value is $S_{int,b}^2$ in Eq. 9 and the standard de-

viation shows its scatter Σ . The detectability of the sources in the intrinsic variance map is then defined by the condition that $S_{int}^2 \geq S_{int,b}^2 + 3\Sigma$. For an illustration (see top of Fig. 3) we present a region around INTEGRAL source IGR J18450-0435 with respective distributions. The green solid area is the distribution in the range $(min, 2m - min)$ with the mean value representing $S_{int,b}^2$ for the current source, and in red the always-positive contribution from the sources in the field is given. The distribution in the range $(min, 2m - min)$ is well fitted by the Gaussian shown with a dashed line. The top of Fig. 3 justifies well the approximate rejection of the source contribution to the overall pixel value distribution in the field. Applying this rejection procedure allows us to obtain the true scatter in the background rather than the scatter in the overall distribution (including sources), which is obviously higher.

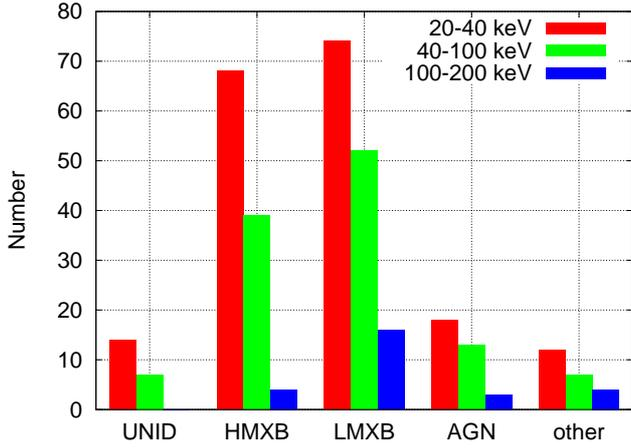


Fig. 4. Number of significantly variable sources detected in different energy bands classified by types.

The detection of variable sources in the innermost region of our Galaxy (circle of 4° from the GC, see Fig. 2) was performed differently because it is a crowded field and therefore a large number of sources contribute to the intrinsic variance background of each other. In contrast to the individual source case, the sources in the inner GC region occupy a significant fraction of the region around the source of interest and therefore influence the m value significantly. This results in improper estimation of the background distribution if one applies the rejection procedure based on $(\min, 2m - \min)$ range (B_1 distribution at the bottom of Fig. 3). In place of calculating the intrinsic variance background and its scatter for each GC source individually, these values were therefore estimated from an empty field near the GC (box at the bottom image of Fig. 2) and assumed to be equal for all the sources in the GC region. The B_2 distribution shown at Fig. 3 (bottom) is accurately determined and well fitted by the Gaussian shown by the dashed line.

5. The catalog of variable sources

The search for variable sources from the reference catalog was performed on the maps generated from ScWs divided into three equal subsequent time periods (maps 1,2, and 3, approximately 2 years each). This was done to detect transient sources that would be difficult (or even impossible) to detect on the map integrated over the whole time period (map T). The search was performed separately on each map (1,2,3) and in each energy band. The results of the search were put into one list from which the sources were selected. Finally, the search was performed on the total map (T) to find sources that were detected only on the map integrated over the whole time period and identify the sources that were active only during specific time periods. The resulting catalog of variable sources detected by *INTEGRAL* can be found in Table 3.

Figure 4 shows the number of significantly variable sources from our catalog for each source type (HMXB, LMXB, AGN, unidentified, and miscellaneous). The majority of the variable sources ($\sim 76\%$) in all energy bands are Galactic X-ray binaries. We see that in the 100-200 keV band there are four times more LMXBs than HMXBs. The remaining variable sources are AGNs ($\sim 10\%$), unidentified ($\sim 7.5\%$), and other ($\sim 6.5\%$) source types (cataclysmic variables, gamma-ray bursts, and pulsars).

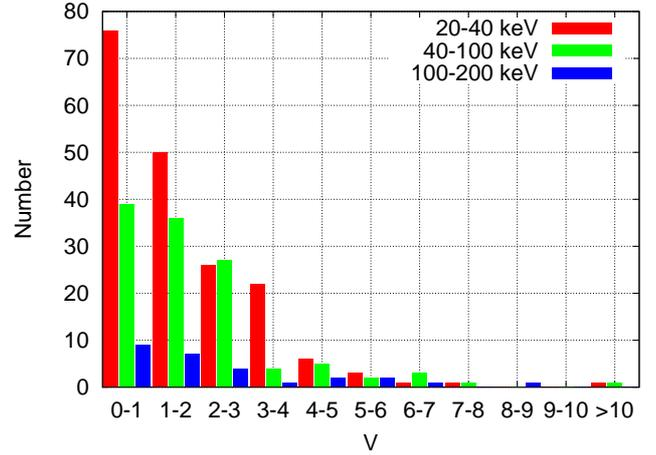


Fig. 5. Number of sources versus fractional variability of the sources detected in different energy bands.

The number of significantly variable sources decreases with energy for each population type, which only reflects the sensitivity of the instruments.

The distribution of the variability of sources from Table 3 is presented in Fig. 5. The variability distribution is approximately normal with one evident outlier, the gamma-ray burst IGR J00245+6251 (Vestrand et al. 2005). However, this is mainly caused by the upper limit to the mean flux of this source being too low. The gamma-ray burst IGR J00245+6251 is detected in all three energy bands. Figure 6 shows the fractional variability in the 40-100 keV band versus the variability in the 20-40 keV band. The majority of the sources that are found to be variable in both the 20-40 keV and 40-100 keV energy bands exhibit nearly equal variability in both bands.

To show the detection threshold for the variability of a source, we compiled a diagram (see Fig. 7) where we plot the fractional variability versus flux for all detected variable sources along with the upper limit to the fractional variability versus flux for all the reference catalog sources detected in our significance map in 20-40 keV energy band. The upper limit was determined by substituting $S_{int,s}^2$ with $S_{int,b}^2 + 3\sigma$ in Eq. (9). Although we chose all the sources detected in our significance map, we used the mean flux of the source because, unlike significance, it is an exposure-independent value. According to our definition, the fractional variability is also an exposure-independent value, so we plot it versus the exposure-independent mean flux to clearly see the detection threshold. We can see that starting from a limiting flux (6.2×10^{-11} ergs/cm²s or ~ 10 mCrab) nearly all catalog sources are found to be variable. The majority of the bright sources are binary systems, which explains why nearly all of them are found to be variable.

We also found a number of variable sources that have no counterparts in the significance map, which means that we were unable to measure the mean flux of these sources as it is compatible with the background mean flux. Hence, we are not able to give their fractional variability value, which is a normalized value and therefore tends to infinity with infinite errors. For these sources, we provide a $3\text{-}\sigma$ lower limit to their fractional variability by taking a $3\text{-}\sigma$ upper limit on their mean flux. Most of the sources are transient, and sometimes (in a specific observation period in a given energy band) the source is not detected in the significance map because the sensitivity of the instrument

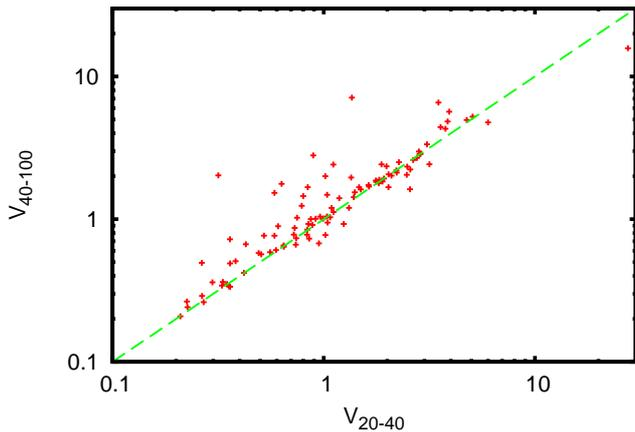


Fig. 6. Fractional variability of sources in the 20-40 keV band versus fractional variability in the 40-100 keV band.

decreases with energy. Therefore, we can see that the variability map provides a tool to detect transient or faint but variable sources that would be missed in mosaics averaged over long timescales. To illustrate the detectability of the sources in the variability map, we provide a list (see Table 1) of the sources that are smeared out in the significance map because of their high exposures. The values given in the table are not normalized

variability values, $V_{r,notorm} = \sqrt{S_{int,s}^2 - S_{int,b}^2}$ along with their $3-\sigma$ errors, Err . To verify that the sources that are absent in the significance maps but detected in the variability maps are not the result of the low detection threshold, we ran the same detection procedures on the mock catalog of 2500 false sources distributed randomly and uniformly over the sky. The test detected 11 of 2500 false sources seen in variability maps and absent from the significance maps, compared to 8 of 576 in the case of the real catalog. This means that our detection criteria are rather strict.

We comment on the inclusion of Crab in our catalog. It is known to be a constant source that is commonly used as a “standard candle” in high-energy astrophysics. There are two reasons why it appears in the catalog. The first is the deterioration of the detector electronics onboard the spacecraft. The loss of detector gain is around 10% over the entire mission. Although this loss is partially compensated by the software, it introduces around 3-5% variability in our method. The remaining variability can be ascribed to systematic errors in the spacecraft alignment (Walter et al. 2003), which for OSA 7.0 are of the order of 7 arcsec (Eckert et al. 2010), hence slightly different positions of the Crab are found in each observation. Since Crab is a very bright source, its Gaussian profile is very steep. When the peak is slightly offset, we measure a sharp decrease in the flux at the catalog position of Crab. The combination of the two effects leads to an artificial variability of Crab in all energy bands. A similar effect occurs in the pixels adjacent to the catalog position of Crab. When the peak of the PSF is found at a slightly displaced position, we find a sharp increase in the flux in this pixel. Our interpretation is confirmed by the image of Crab in the variability map, where the closest pixels to the source are found to be very variable, creating a ring-like structure. Moreover, it has been found that the observed position of Crab does not coincide with the position of the pulsar (Eckert et al. 2010), which thus explains such an effect at the expected source position. To determine the influence of this effect on other sources, we inspected

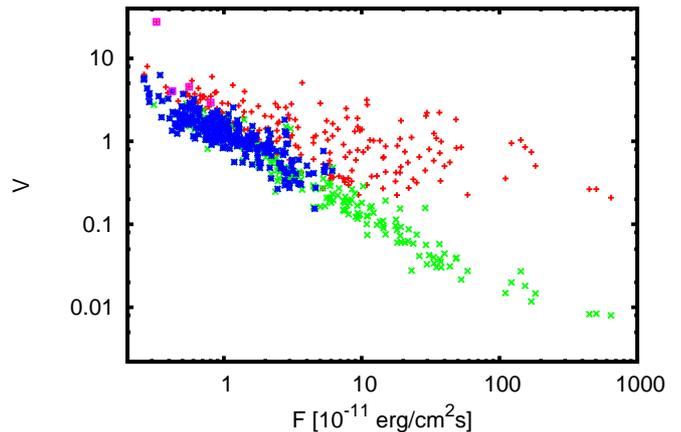


Fig. 7. Fractional variability (V) versus flux (F) for all significantly variable sources (red crosses) from Table 3. Energy band is 20-40 keV. For comparison, the green crosses show the fractional variability detection threshold ($3-\sigma$) versus flux for all reference catalog sources detected in the significance map. The sources not detected at the variability map are indicated by blue stars and are coincident with their green cross counterparts. Pink squares indicate $3-\sigma$ lower limits to the fractional variability of the sources that are not detected in the significance map.

the 11 brightest sources in the 20-40 keV band and looked for a similar situation. In the case of Cyg X-1 and Sco X-1, the same effect, albeit weaker, was also seen. However, the derived value of their variability was not found to be affected by this effect. This effect contributes mainly to the variability of the pixels around the catalog position of these sources. Cyg X-1 and Sco X-1 are intrinsically very variable so the value extracted from the source position is much higher than for surrounding pixels, which is the opposite of the situation found in the Crab. For all the other sources, the influence of the misalignment was found to be negligible.

Finally, we performed a test to find cases in which a source is coincident with the ghost of another source within one ScW (a case described in Sect. 3). We considered all the reference catalog sources and searched for “ghost-source” pairs in individual ScWs from the list used for our all-sky maps. If one of the sources in a given pair was present in our variability catalog, the pair was selected for further analysis. According to our simulations, if two sources are in the ghosts of each other, the fainter one loses up to half of its flux to the flux of the brighter one. If one of the sources is substantially brighter than the other, the relative distortion of the flux of the bright source is minor. Therefore, the flux of the source is significantly distorted if its “ghost companion” is brighter or comparable in brightness to the source itself. In the latter case, the “ghost companion” is also affected. Thus, we assume that if the source in the ghost is more than ten times fainter than its “ghost companion”, its contaminating influence is negligible, whereas its own flux is contaminated significantly. After adopting this condition, we obtained a list of the sources affected by such position coincidences and the exposure times for each of them during which they were affected. For nearly all of the sources from the list, the fraction of exposures with distorted flux is less than 1%, which infers a relative uncertainty in the average flux and fractional variability of the same order. This is much smaller than the error set on variability

in our catalog and, as can be seen from the Fig. 7 is smaller than the variability detection threshold even for the brightest sources. Nonetheless, a number of sources have larger than 1% errors induced by the ghosts, which we indicate with a ^s superscript in the catalog and provide a Table 2 where both errors are given. As can be seen, in all cases the ghost induced error is much smaller than the catalog variability error.

6. The All-Sky online

To make our results available to the community, we decided to take advantage of the SkyView interface (McGlynn et al. 1998) (i.e., a Virtual Observatory service available online⁴ developed at and hosted by the High Energy Astrophysics Science Archive Research Centre (HEASARC)). SkyView provides a straightforward interface where users can retrieve images of the sky at all wavelengths from radio to gamma-rays (McGlynn et al. 1998). SkyView uses NED and SIMBAD name resolvers to translate names into positions and is connected to the HEASARC catalog services. The user can retrieve images in various coordinate systems, projections, scalings, and sizes as ordinary FITS as well as standard JPEG and GIF file formats. The output image is centered on the queried object or sky position. SkyView is also available as a standalone Java application (McGlynn et al. 1997). The ease-of-use of this system allowed us to incorporate INTEGRAL/ISGRI variability and significance all-sky maps into the SkyView interface. We developed a simple web interface for the SkyView Java application and have made all-sky mosaics available online.

7. Concluding remarks

Our study of variability of the *INTEGRAL* sky has found that 202 sources exhibit significantly variable hard X-ray emission. To compile the catalog of variable sources, we have developed and implemented a method to detect variable sources, and compiled all-sky variability maps. A search for variable sources from the *INTEGRAL* reference catalog was carried out in three energy bands: 20-40, 40-100, and 100-200 keV. The variable sources were detected in all studied energy bands, although their number sharply decreases with increasing energy. A number of sources were detected only during specific time periods and not detected on the map integrated over the whole time period. These sources are most likely transient. On the other hand, some sources were found to be variable only on the total variability map. This means that they might be persistent and not extremely variable sources.

We found that around 76% of all variable sources of our catalog are binary systems and nearly 24% of variable sources are either AGNs, unidentified, or other source types. The variability measurements of our catalog sources have rather normal distributions in all energy bands. We found that in the majority of cases the variability of the source in the first band correlates with its variability in the second band. We derived the limits to the fractional variability value to be detected as a function of the source flux (Fig. 7). We also found that variability map can be a tool to detecting transient or faint but variable sources that would be missed in mosaics averaged over long timescales. In a forthcoming paper, we will discuss in more detail the properties of the variable sources detected during this study in order to gain some physical insights into the population of hard X-ray sources.

Finally, we emphasize that the sky maps generated during this study represent 6 years of *INTEGRAL* operation in orbit. In addition to the variability maps, we have compiled significance maps in three energy bands (20-40, 40-100, and 100-200 keV). All our maps are available as an online service to the community using the SkyView engine.

Acknowledgements

Based on observations with INTEGRAL, an ESA project with instruments and science data centre funded by ESA member states (especially the PI countries: Denmark, France, Germany, Italy, Switzerland, Spain), Czech Republic and Poland, and with participation of Russia and the USA.

This work was supported by the Swiss National Science Foundation and the Swiss Agency for Development and Cooperation in the framework of the programme SCOPES - Scientific co-operation between Eastern Europe and Switzerland. The computational part of the work was done at VIRGO.UA⁵ and BITP⁶ computing resources.

We are grateful to the anonymous referee for the critical remarks which helped us improve the paper.

IT acknowledges the support from the INTAS YSF grant No. 06-100014-6348.

Appendix: Error Calculation on V_r

We use the standard error propagation formula to find the error, σ_{V_r} , of the function $V_r = f(S_{int,s}^2 = a, S_{int,b}^2 = b, F_s = c, F_b = d)$ so :

$$\sigma_{V_r} = \sigma_f = \sqrt{\left(\frac{\partial f}{\partial a}\sigma_a\right)^2 + \left(\frac{\partial f}{\partial b}\sigma_b\right)^2 + \left(\frac{\partial f}{\partial c}\sigma_c\right)^2 + \left(\frac{\partial f}{\partial d}\sigma_d\right)^2}, \quad (10)$$

where $\sigma_a = \sigma_b = \Sigma$ and $\sigma_c = \sigma_d = \sigma$ for a given source. By substituting the appropriate values in Eq. 10 and by taking derivatives we find that:

$$\sigma_{V_r} = \sqrt{\frac{\Sigma^2}{2(F_s - F_b)^2(S_{int,s}^2 - S_{int,b}^2)} + \frac{2\sigma^2(S_{int,s}^2 - S_{int,b}^2)}{(F_s - F_b)^4}}. \quad (11)$$

References

- Almaini, O., Lawrence, A., Shanks, T., et al. 2000, MNRAS, 315, 325
 Arévalo, P. & Uttley, P. 2006, MNRAS, 367, 801
 Barlow, E. J., Knigge, C., Bird, A. J., et al. 2006, MNRAS, 372, 224
 Barnard, R., Kolb, U. C., & Osborne, J. P. 2002, ArXiv Astrophysics e-prints
 Bassani, L., Malizia, A., Stephen, J. B., & INTEGRAL AGNs Survey Team. 2007, in ESA Special Publication, Vol. 622, ESA Special Publication, 165–+
 Bazzano, A., Stephen, J. B., Fiocchi, M., et al. 2006, ApJ, 649, L9
 Beckmann, V., Barthelmy, S. D., Courvoisier, T., et al. 2007, A&A, 475, 827
 Beckmann, V., Gehrels, N., Shrader, C. R., & Soldi, S. 2006, ApJ, 638, 642
 Beckmann, V., Soldi, S., Ricci, C., et al. 2009, A&A, 505, 417
 Bélanger, G., Goldwurm, A., Goldoni, P., et al. 2004, ApJ, 601, L163
 Bélanger, G., Goldwurm, A., Renaud, M., et al. 2006, ApJ, 636, 275
 Bird, A. J., Bazzano, A., Bassani, L., et al. 2010, ApJS, 186, 1
 Bird, A. J., Malizia, A., Bazzano, A., et al. 2007, ApJS, 170, 175
 Bodaghee, A., Courvoisier, T. J.-L., Rodriguez, J., et al. 2007, A&A, 467, 585
 Bouchet, L., Roques, J. P., Mandrou, P., et al. 2005, ApJ, 635, 1103
 Courvoisier, T. J.-L., Walter, R., Beckmann, V., et al. 2003, A&A, 411, L53
 den Hartog, P. R., Hermsen, W., Kuiper, L., et al. 2006, A&A, 451, 587

⁵ <http://virgo.org.ua>

⁶ <http://bitp.kiev.ua>

⁴ <http://skyview.gsfc.nasa.gov>

- Ducci, L., Sidoli, L., Mereghetti, S., Paizis, A., & Romano, P. 2009, *MNRAS*, 398, 2152
- Ebisawa, K., Bourban, G., Bodaghee, A., Mowlavi, N., & Courvoisier, T. J.-L. 2003, *A&A*, 411, L59
- Eckert, D., Produit, N., Paltani, S., Neronov, A., & Courvoisier, T. J.-L. 2008, *A&A*, 479, 27
- Eckert, D., Savchenko, V., Produit, N., & Ferrigno, C. 2010, *A&A*, 509, A33+
- Götz, D., Mereghetti, S., Merlini, D., Sidoli, L., & Belloni, T. 2006, *A&A*, 448, 873
- Gros, A., Goldwurm, A., Cadolle-Bel, M., et al. 2003, *A&A*, 411, L179
- Ishibashi, W. & Courvoisier, T. 2009, *A&A*, 504, 61
- Krivonos, R., Revnivtsev, M., Churazov, E., et al. 2007, *A&A*, 463, 957
- Lebrun, F., Leray, J. P., Lavocat, P., et al. 2003, *A&A*, 411, L141
- Lebrun, F., Roques, J., Sauvageon, A., et al. 2005, *Nuclear Instruments and Methods in Physics Research A*, 541, 323
- Liang, E. W. & Liu, H. T. 2003, *MNRAS*, 340, 632
- Lund, N., Budtz-Jørgensen, C., Westergaard, N. J., et al. 2003, *A&A*, 411, L231
- Mas-Hesse, J. M., Giménez, A., Culhane, J. L., et al. 2003, *A&A*, 411, L261
- McGlynn, T., Scollick, K., & White, N. 1998, in *IAU Symposium*, Vol. 179, *New Horizons from Multi-Wavelength Sky Surveys*, ed. B. J. McLean, D. A. Golombek, J. J. E. Hayes, & H. E. Payne, 465–+
- McGlynn, T. A., Scollick, K. A., & White, N. E. 1997, in *Astronomical Society of the Pacific Conference Series*, Vol. 125, *Astronomical Data Analysis Software and Systems VI*, ed. G. Hunt & H. Payne, 337–+
- Molkov, S. V., Cherepashchuk, A. M., Lutovinov, A. A., et al. 2004, *Astronomy Letters*, 30, 534
- Nandra, K., George, I. M., Mushotzky, R. F., Turner, T. J., & Yaqoob, T. 1997, *ApJ*, 476, 70
- Nevalainen, J., Eckert, D., Kaastra, J., Bonamente, M., & Kettula, K. 2009, *A&A*, 508, 1161
- Revnivtsev, M. G., Sunyaev, R. A., Varshalovich, D. A., et al. 2004, *Astronomy Letters*, 30, 382
- Romano, P., Sidoli, L., Cusumano, G., et al. 2009, *MNRAS*, 1437
- Sazonov, S., Revnivtsev, M., Krivonos, R., Churazov, E., & Sunyaev, R. 2007, *A&A*, 462, 57
- Ubertini, P., Lebrun, F., Di Cocco, G., et al. 2003, *A&A*, 411, L131
- Uttley, P. 2004, *MNRAS*, 347, L61
- Vedrenne, G., Roques, J.-P., Schönfelder, V., et al. 2003, *A&A*, 411, L63
- Vestrand, W. T., Wozniak, P. R., Wren, J. A., et al. 2005, *Nature*, 435, 178
- Walter, R., Favre, P., Dubath, P., et al. 2003, *A&A*, 411, L25
- Winkler, C., Courvoisier, T. J.-L., Di Cocco, G., et al. 2003, *A&A*, 411, L1

Table 1. The transient sources detected at the intrinsic variance map and not detected at the significance map.

Name	Class	$V_{r,normal} \pm Err$ (c/s)	Exposure (ksec)	Map	Band
IGR J00245+6251	GRB	2.003 ± 0.006	1522.2	2	20-40
IGR J00245+6251	GRB	1.455 ± 0.016	1771.9	2,3	40-100
IGR J00245+6251	GRB	0.340 ± 0.017	1522.2	2	100-200
RX J0137.7+5814	UNID	0.319 ± 0.166	2477.1	T	20-40
IGR J08408-4503	HMXB	0.199 ± 0.127	2945.0	T	20-40
IGR J11098-6457	AGN	0.408 ± 0.096	423.0	3	40-100
IGR J11321-5311	HMXB	0.383 ± 0.066	870.5	2	40-100
IGR J11321-5311	HMXB	0.226 ± 0.051	870.5	2	100-200
HR 4492	UNID	0.571 ± 0.045	1012.5	1	20-40
PKS 1241-399	AGN	0.405 ± 0.274	1312.7	T	20-40
IGR J16248-4603	UNID	0.486 ± 0.101	917.8	3	40-100

Table 2. Sources with additional error induced by the “ghosts”.

Name	20-40 keV					40-100 keV					100-200 keV				
	V_r	$V_{r,err}$	G_{err}	Gexp	Exp	V_r	$V_{r,err}$	G_{err}	Gexp	Exp	V_r	$V_{r,err}$	G_{err}	Gexp	Exp
PSR B1509-58	0.338	0.048	0.011	12.0	1054.6	ND	ND	ND	ND	ND	ND	ND	ND	ND	ND
IGR J16493-4348	1.392	0.382	0.011	27.0	2349.7	ND	ND	ND	ND	ND	ND	ND	ND	ND	ND
4U 1543-624	1.049	0.425	0.013	9.0	716.7	ND	ND	ND	ND	ND	ND	ND	ND	ND	ND
XTE J1807-294	3.492	1.143	0.032	159.0	4925.0	ND	ND	ND	ND	ND	ND	ND	ND	ND	ND
IGR J17597-2201	0.608	0.049	0.020	108.0	5355.6	0.892	0.105	0.020	108.0	5355.6	ND	ND	ND	ND	ND
IGR J16351-5806	ND	ND	ND	ND	ND	< 2.720	0.000	0.022	24.0	1098.9	ND	ND	ND	ND	ND
4U 1705-32	ND	ND	ND	ND	ND	1.667	0.512	0.035	135.0	3839.1	ND	ND	ND	ND	ND
XTE J1818-245	3.495	0.987	0.039	324.0	8391.2	6.571	0.000	0.076	324.0	4246.5	ND	ND	ND	ND	ND
IGR J17464-3213	3.165	0.041	0.018	225.0	12428.2	2.427	0.058	0.018	225.0	12428.2	1.567	0.164	0.028	240.0	8521.1

Here, V_r is the true fractional variability of the source, $V_{r,err}$ is the fractional variability error same as in catalog, G_{err} is the error induced by the source, Gexp, in ksec, is the exposure time the source was affected by the “ghost”, Exp, in ksec, is the total exposure time.

Table 3. The catalog of variable sources detected by *INTEGRAL*

Nr.	Name	20-40 keV			40-100 keV			100-200 keV			Class
		V	F (10^{-11} ergs s $^{-1}$ cm $^{-2}$)	E (ksec)	V	F (10^{-11} ergs s $^{-1}$ cm $^{-2}$)	E (ksec)	V	F (10^{-11} ergs s $^{-1}$ cm $^{-2}$)	E (ksec)	
1	IGR J00245+6251	> 27.579 ^{2*}	< 0.324	1522.2	> 15.784 ^{2*,3*}	< 0.852	1771.9	> 6.324 ^{2*}	< 1.957	1522.2	GRB
2	IGR J00291+5934	2.845 ± 0.360 ²	2.369 ± 0.212	1681.1	2.858 ± 0.558 ²	3.345 ± 0.462	1681.1	ND	ND	0.0	LMXB
3	IGR J00370+6122	> 4.019 ^{1*}	< 0.423	812.0	ND	ND	0.0	ND	ND	0.0	HMXB
4	SMC X-1	0.647 ± 0.040 ¹	26.196 ± 1.155	56.5	0.641 ± 0.339 ¹	6.669 ± 2.419	56.5	ND	ND	0.0	HMXB
5	3A 0114+650	1.404 ± 0.064 ^{1,2,3}	6.718 ± 0.210	2295.6	1.542 ± 0.215 ^{1,2,3}	4.702 ± 0.447	2295.6	ND	ND	0.0	HMXB
6	H 0115+634	1.832 ± 0.017 ^{1,3}	48.370 ± 0.318	961.5	1.890 ± 0.107 ^{1,3}	16.680 ± 0.665	961.5	ND	ND	0.0	HMXB
7	4U 0142+614	1.383 ± 0.858 ³	1.402 ± 0.603	245.1	ND	ND	0.0	ND	ND	0.0	HMXB
8	RX J0146.9+6121	1.248 ± 0.523 ¹	1.749 ± 0.501	626.9	ND	ND	0.0	ND	ND	0.0	HMXB
9	IGR J01583+6713	3.482 ± 3.303 ²	0.565 ± 0.378	999.8	ND	ND	0.0	ND	ND	0.0	HMXB
10	NGC 788	0.599 ± 0.131 ³	2.996 ± 0.398	468.0	ND	ND	0.0	ND	ND	0.0	AGN
11	SWIFT J0216.3+5128	> 2.926 ^{2*}	< 0.801	750.4	ND	ND	0.0	ND	ND	0.0	AGN
12	NGC 1052	ND	ND	0.0	> 2.593 ^{1*}	< 1.265	607.0	ND	ND	0.0	AGN
13	NGC 1365	1.435 ± 0.866 ²	2.102 ± 0.876	188.9	ND	ND	0.0	ND	ND	0.0	AGN
14	EXO 0331+530	0.741 ± 0.004 ²	170.496 ± 0.644	333.0	0.735 ± 0.045 ²	31.100 ± 1.332	333.0	ND	ND	0.0	HMXB
15	X Per	0.419 ± 0.018 ^{1,3}	19.009 ± 0.437	792.8	0.420 ± 0.028 ^{1,3}	29.324 ± 0.942	792.8	ND	ND	0.0	HMXB
16	LMC X-4	1.388 ± 0.075 ^{1,3}	10.026 ± 0.376	412.9	1.426 ± 0.534 ¹	3.075 ± 0.808	349.5	ND	ND	0.0	HMXB
17	Crab	> 0.209 ^{1,2,3}	< 645.163	1591.8	> 0.208 ^{1,2,3}	< 780.058	1591.8	0.212 ± 0.001 ^{1,2,3}	529.148 ± 1.576	1591.8	SNR
18	H 0614+091	0.428 ± 0.045 ^{1,2,3}	14.917 ± 0.468	2065.7	0.668 ± 0.116 ^{1,2}	13.048 ± 1.152	974.1	ND	ND	0.0	LMXB
19	3A 0656-072	1.292 ± 0.130 ³	5.416 ± 0.385	560.3	ND	ND	0.0	ND	ND	0.0	HMXB
20	EXO 0748-676	0.270 ± 0.026 ^{1,3}	14.279 ± 0.595	546.5	0.262 ± 0.062 ³	17.019 ± 2.283	68.8	ND	ND	0.0	LMXB
21	Ginga 0836-429	1.113 ± 0.015 ¹	23.026 ± 0.218	1360.8	1.121 ± 0.029 ¹	24.152 ± 0.437	1360.8	1.326 ± 0.359 ¹	6.269 ± 1.160	1360.8	LMXB
22	Vela X-1	0.853 ± 0.001 ^{1,2,3}	153.607 ± 0.167	3413.2	0.730 ± 0.008 ^{1,2,3}	46.951 ± 0.338	3413.2	ND	ND	0.0	HMXB
23	GRO J1008-57	2.569 ± 0.341 ^{1,2}	2.473 ± 0.231	2126.4	2.230 ± 0.935 ¹	1.817 ± 0.536	1049.8	ND	ND	0.0	HMXB
24	IGR J10101-5654	> 3.170 ^{2*}	< 0.762	1096.9	ND	ND	0.0	ND	ND	0.0	HMXB
25	4U 1036-56	1.924 ± 0.687 ^{1,3}	0.938 ± 0.224	1372.9	ND	ND	0.0	ND	ND	0.0	HMXB
26	Mrk 421	0.646 ± 0.019 ^{2,3}	14.443 ± 0.290	1190.2	0.655 ± 0.041 ²	17.456 ± 0.773	515.1	ND	ND	0.0	AGN
27	IGR J11098-6457	ND	ND	0.0	> 2.023 ^{3*}	< 1.865	423.0	ND	ND	0.0	AGN
28	Cen X-3	0.994 ± 0.008 ^{1,2,3}	37.787 ± 0.207	2188.2	1.007 ± 0.147 ^{1,2,3}	4.961 ± 0.422	2188.2	ND	ND	0.0	HMXB
29	IGR J11215-5952	> 3.736 ^{1,2*}	< 0.613	1774.7	ND	ND	0.0	ND	ND	0.0	HMXB
30	IGR J11305-6256	> 0.959 ^{1,2,3*}	< 2.205	2193.3	ND	ND	0.0	ND	ND	0.0	HMXB
31	IGR J11321-5311	ND	ND	0.0	> 3.119 ^{2*}	< 1.135	870.5	> 2.651 ^{2*}	< 3.106	870.5	HMXB
32	HR 4492	> 4.555 ^{1*}	< 0.559	1012.5	ND	ND	0.0	ND	ND	0.0	UNID
33	IGR J11435-6109	0.961 ± 0.107 ²	4.467 ± 0.348	672.4	1.041 ± 0.312 ²	3.475 ± 0.714	672.4	ND	ND	0.0	HMXB
34	1E 1145.1-6141	0.870 ± 0.019 ^{1,2,3}	14.913 ± 0.222	2367.0	1.002 ± 0.063 ^{1,2,3}	10.579 ± 0.447	2367.0	ND	ND	0.0	HMXB
35	H 1145-619	1.723 ± 0.335 ¹	2.513 ± 0.345	1112.7	ND	ND	0.0	ND	ND	0.0	HMXB
36	IGR J12042-0756	ND	ND	0.0	> 2.536 ^{3*}	< 2.663	299.8	ND	ND	0.0	AGN
37	NGC 4151	0.738 ± 0.036 ^{1,2,3}	8.179 ± 0.225	1883.9	0.662 ± 0.053 ^{1,2,3}	12.689 ± 0.504	1883.9	ND	ND	0.0	AGN
38	NGC 4388	0.330 ± 0.044 ^{1,2}	8.433 ± 0.307	1672.6	0.342 ± 0.074 ^{1,2}	13.156 ± 0.652	1672.6	ND	ND	0.0	AGN
39	GX 301-2	0.949 ± 0.003 ^{1,2,3}	122.223 ± 0.239	2586.3	0.676 ± 0.031 ^{1,2,3}	16.475 ± 0.477	2586.3	ND	ND	0.0	HMXB
40	3C 273	0.297 ± 0.029 ^{1,2,3}	8.042 ± 0.172	2556.9	0.361 ± 0.050 ^{1,2,3}	11.674 ± 0.374	2556.9	ND	ND	0.0	AGN
41	1H 1249-637	> 3.187 ^{3*}	< 0.674	910.1	ND	ND	0.0	ND	ND	0.0	HMXB
42	3A 1246-588	0.416 ± 0.082 ²	3.635 ± 0.362	924.5	ND	ND	0.0	ND	ND	0.0	LMXB
43	3C 279	ND	ND	0.0	2.163 ± 1.193 ²	1.508 ± 0.572	1434.5	ND	ND	0.0	AGN
44	NGC 4945	0.360 ± 0.053 ^{1,2,3}	7.998 ± 0.263	2821.4	0.336 ± 0.069 ^{1,2,3}	14.424 ± 0.547	2821.4	0.881 ± 0.307 ¹	10.756 ± 2.390	801.2	AGN

Table 3. continued.

Nr.	Name	20-40 keV			40-100 keV			100-200 keV			Class
		V	F (10^{-11} ergs s^{-1} cm^{-2})	E (ksec)	V	F (10^{-11} ergs s^{-1} cm^{-2})	E (ksec)	V	F (10^{-11} ergs s^{-1} cm^{-2})	E (ksec)	
45	IGR J13091+1137	> 2.685 ^{1*}	< 1.281	547.8	ND	ND	0.0	ND	ND	0.0	AGN
46	NGC 5033	ND	ND	0.0	> 2.675 ^{1*}	< 1.320	698.0	ND	ND	0.0	AGN
47	Cen A	0.349 ± 0.007 ^{1,2,3}	23.707 ± 0.241	2330.7	0.350 ± 0.011 ^{1,2,3}	35.375 ± 0.516	2330.7	0.395 ± 0.070 ^{1,3}	29.876 ± 1.567	1757.8	AGN
48	4U 1323-62	0.585 ± 0.047 ^{1,2,3}	5.844 ± 0.228	2569.7	0.765 ± 0.153 ^{1,2,3}	5.321 ± 0.468	2569.7	ND	ND	0.0	LMXB
49	MCG-06-30-015	1.579 ± 0.738 ¹	1.056 ± 0.340	663.7	ND	ND	0.0	> 2.991 ^{1*}	< 2.992	663.7	AGN
50	IC 4329A	0.521 ± 0.056 ^{1,3}	5.883 ± 0.304	1333.4	0.766 ± 0.147 ¹	6.614 ± 0.842	646.9	ND	ND	0.0	AGN
51	IGR J14003-6326	> 2.621 ^{2*}	< 0.779	690.8	ND	ND	0.0	ND	ND	0.0	UNID
52	Circinus Galaxy	0.227 ± 0.025 ^{1,3}	9.493 ± 0.272	1516.8	ND	ND	0.0	ND	ND	0.0	AGN
53	PSR B1509-58 ^g	0.338 ± 0.048 ²	5.927 ± 0.400	1054.6	ND	ND	0.0	ND	ND	0.0	SNR
54	Cir X-1	1.108 ± 0.080 ^{1,2,3}	4.474 ± 0.207	3758.3	ND	ND	0.0	ND	ND	0.0	LMXB
55	H 1538-522	0.632 ± 0.013 ^{1,2,3}	14.329 ± 0.185	4749.1	1.768 ± 0.998 ³	3.039 ± 1.173	1069.5	ND	ND	0.0	HMXB
56	XTE J1543-568	> 3.448 ^{1,3*}	< 0.718	2474.4	ND	ND	0.0	ND	ND	0.0	HMXB
57	4U 1543-624^g	1.049 ± 0.425 ²	1.797 ± 0.485	716.7	ND	ND	0.0	ND	ND	0.0	LMXB
58	AX J1550.8-5418	> 3.611 ^{1*,3}	< 0.534	2725.9	ND	ND	0.0	ND	ND	0.0	LMXB
59	XTE J1550-564	2.209 ± 0.032 ¹	29.752 ± 0.308	1511.0	2.196 ± 0.033 ¹	56.789 ± 0.611	1511.0	2.082 ± 0.108 ¹	44.222 ± 1.618	1511.0	LMXB
60	H 1608-522	1.349 ± 0.036 ^{1,2,3}	9.703 ± 0.180	4193.8	1.959 ± 0.124 ^{1,2,3}	8.120 ± 0.358	4193.8	1.418 ± 0.411 ²	7.190 ± 1.430	1659.8	LMXB
61	IGR J16195-4945	1.451 ± 0.447 ^{1,2,3}	1.179 ± 0.172	4478.2	ND	ND	0.0	ND	ND	0.0	HMXB
62	IGR J16194-2810	2.263 ± 1.096 ¹	1.401 ± 0.467	1214.1	ND	ND	0.0	ND	ND	0.0	LMXB
63	Sco X-1	> 0.265 ^{1,2,3}	< 449.583	1627.5	0.494 ± 0.039 ^{1,2,3}	16.011 ± 0.519	1627.5	ND	ND	0.0	LMXB
64	IGR J16207-5129	1.143 ± 0.181 ^{1,2,3}	2.206 ± 0.177	4166.5	ND	ND	0.0	ND	ND	0.0	HMXB
65	IGR J16248-4603	ND	ND	0.0	> 3.039 ^{3*}	< 1.480	917.8	ND	ND	0.0	UNID
66	SWIFT J1626.6-5156	> 3.841 ^{2*}	< 0.391	1614.9	ND	ND	0.0	ND	ND	0.0	UNID
67	IGR J16283-4838	2.258 ± 0.800 ^{2,3}	0.961 ± 0.222	2520.1	ND	ND	0.0	ND	ND	0.0	HMXB
68	IGR J16318-4848	1.073 ± 0.014 ^{1,2,3}	19.002 ± 0.172	4304.5	1.030 ± 0.044 ^{1,2,3}	12.066 ± 0.337	4304.5	ND	ND	0.0	HMXB
69	IGR J16320-4751	0.836 ± 0.020 ^{1,2,3}	11.067 ± 0.171	4406.7	0.845 ± 0.169 ^{1,2,3}	4.536 ± 0.334	4406.7	ND	ND	0.0	HMXB
70	4U 1626-67	0.377 ± 0.035 ^{2,3}	11.789 ± 0.500	1016.9	ND	ND	0.0	ND	ND	0.0	LMXB
71	IGR J16328-4726	2.269 ± 0.389 ^{1,2}	1.588 ± 0.183	3686.7	2.506 ± 0.955 ¹	1.935 ± 0.516	1867.1	ND	ND	0.0	UNID
72	4U 1630-47	1.244 ± 0.014 ¹	33.502 ± 0.271	1869.6	0.925 ± 0.020 ¹	33.887 ± 0.516	1869.6	0.812 ± 0.099 ¹	16.736 ± 1.353	1869.6	LMXB
73	IGR J16351-5806^g	ND	ND	0.0	> 2.720 ^{2*}	< 1.109	1098.9	ND	ND	0.0	AGN
74	IGR J16358-4726	3.978 ± 1.084 ¹	1.412 ± 0.271	1842.8	ND	ND	0.0	ND	ND	0.0	HMXB
75	IGR J16393-4643	0.688 ± 0.125 ^{1,2,3}	3.622 ± 0.172	4594.9	ND	ND	0.0	ND	ND	0.0	HMXB
76	H 1636-536	0.748 ± 0.010 ^{1,2,3}	20.582 ± 0.196	3418.8	1.023 ± 0.041 ^{1,2,3}	14.417 ± 0.387	3418.8	1.398 ± 0.534 ¹	5.944 ± 1.532	1433.9	LMXB
77	IGR J16418-4532	1.107 ± 0.122 ^{1,2,3}	3.036 ± 0.173	5157.6	ND	ND	0.0	ND	ND	0.0	HMXB
78	GX 340+0	0.554 ± 0.007 ^{1,2,3}	21.683 ± 0.174	5108.7	ND	ND	0.0	ND	ND	0.0	LMXB
79	IGR J16465-4507	1.951 ± 0.572 ¹	1.371 ± 0.276	2088.5	ND	ND	0.0	> 4.206 ^{1*}	< 2.032	2088.5	HMXB
80	IGR J16479-4514	1.879 ± 0.166 ^{1,2,3}	2.984 ± 0.175	5331.1	2.421 ± 0.629 ^{1,2,3}	2.074 ± 0.336	5331.1	ND	ND	0.0	HMXB
81	IGR J16493-4348 ^g	1.392 ± 0.382 ²	1.494 ± 0.266	2349.7	ND	ND	0.0	ND	ND	0.0	HMXB
82	GRO J1655-40	1.771 ± 0.037 ²	19.291 ± 0.282	3450.1	1.828 ± 0.046 ²	29.777 ± 0.533	3450.1	1.836 ± 0.172 ²	23.010 ± 1.421	3450.1	LMXB
83	IGR J16558-4150	ND	ND	0.0	> 6.632 ^{1*}	< 0.744	3418.6	ND	ND	0.0	UNID
84	Her X-1	0.847 ± 0.008 ^{2,3}	52.803 ± 0.367	474.7	0.926 ± 0.117 ^{2,3}	9.388 ± 0.812	474.7	ND	ND	0.0	LMXB
85	OA0 1657-415	0.834 ± 0.004 ^{1,2,3}	48.793 ± 0.174	8861.0	0.779 ± 0.014 ^{1,2,3}	31.754 ± 0.323	8861.0	ND	ND	0.0	HMXB
86	XTE J1701-462	1.167 ± 0.088 ^{2,3}	4.656 ± 0.236	3036.8	ND	ND	0.0	ND	ND	0.0	LMXB
87	GX 339-4	2.029 ± 0.019 ^{1,2,3}	29.318 ± 0.191	3916.5	2.061 ± 0.029 ^{1,2,3}	37.574 ± 0.368	3916.5	1.888 ± 0.136 ^{1,2,3}	19.639 ± 0.980	3916.5	LMXB
88	4U 1700-377	1.037 ± 0.002 ^{1,2,3}	142.908 ± 0.155	11696.8	1.045 ± 0.004 ^{1,2,3}	105.130 ± 0.284	11696.8	1.236 ± 0.134 ^{1,2,3}	25.588 ± 0.745	11696.8	HMXB

Table 3. continued.

Nr.	Name	20-40 keV			40-100 keV			100-200 keV			Class
		V	F (10^{-11} ergs s^{-1} cm^{-2})	E (ksec)	V	F (10^{-11} ergs s^{-1} cm^{-2})	E (ksec)	V	F (10^{-11} ergs s^{-1} cm^{-2})	E (ksec)	
89	GX 349+2	$0.445 \pm 0.026^{1,2,3}$	28.934 ± 0.145	11912.8	ND	ND	0.0	ND	ND	0.0	LMXB
90	H 1702-429	$1.038 \pm 0.025^{1,2,3}$	11.497 ± 0.175	7731.6	$1.481 \pm 0.087^{1,2,3}$	8.900 ± 0.327	7731.6	ND	ND	0.0	LMXB
91	4U 1705-32^s	ND	ND	0.0	1.667 ± 0.512^2	2.266 ± 0.427	3839.1	ND	ND	0.0	LMXB
92	IGR J17088-4008	3.498 ± 2.326^3	0.709 ± 0.325	2654.6	ND	ND	0.0	ND	ND	0.0	LMXB
93	H 1705-440	$1.018 \pm 0.020^{1,2,3}$	13.569 ± 0.180	6747.6	$2.001 \pm 0.164^{1,2,3}$	6.127 ± 0.339	6747.6	ND	ND	0.0	LMXB
94	IGR J17091-3624	ND	ND	0.0	$1.612 \pm 0.184^{1,2}$	4.985 ± 0.290	8825.8	3.300 ± 0.986^1	5.201 ± 0.981	4820.5	LMXB
95	XTE J1709-267	$3.577 \pm 1.289^{1,3}$	0.674 ± 0.151	8605.2	4.418 ± 2.617^3	1.157 ± 0.472	3714.3	ND	ND	0.0	LMXB
96	IGR J17098-3628	2.562 ± 0.395^2	2.814 ± 0.239	3993.2	$1.622 \pm 0.143^{1,2}$	5.875 ± 0.289	8820.5	ND	ND	0.0	LMXB
97	IGR J17195-4100	1.361 ± 0.314^1	1.812 ± 0.253	4014.1	7.114 ± 6.035^1	0.761 ± 0.452	4014.1	ND	ND	0.0	CV
98	XTE J1720-318	2.654 ± 0.361^1	1.781 ± 0.170	4940.9	2.601 ± 0.436^1	2.649 ± 0.307	4940.9	ND	ND	0.0	LMXB
99	IGR J17204-3554	ND	ND	0.0	3.686 ± 1.659^1	1.129 ± 0.347	4845.8	ND	ND	0.0	AGN
100	IGR J17252-3616	$1.162 \pm 0.040^{1,2,3}$	6.147 ± 0.123	12090.8	ND	ND	0.0	ND	ND	0.0	HMXB
101	4U 1722-30	$0.383 \pm 0.013^{1,2,3}$	12.906 ± 0.103	12720.4	$0.507 \pm 0.046^{1,2,3}$	12.061 ± 0.193	12720.4	ND	ND	0.0	LMXB
102	IGR J17285-2922	ND	ND	0.0	$> 6.885^{3*}$	< 0.562	3750.0	ND	ND	0.0	UNID
103	3A 1728-169	$0.445 \pm 0.075^{1,2,3}$	8.496 ± 0.151	12403.3	ND	ND	0.0	ND	ND	0.0	LMXB
104	GX 354-0	$0.800 \pm 0.004^{1,2,3}$	30.897 ± 0.107	12420.7	$1.450 \pm 0.030^{1,2,3}$	14.648 ± 0.201	12420.7	ND	ND	0.0	LMXB
105	GX 1+4	$0.722 \pm 0.003^{1,2,3}$	36.923 ± 0.105	13270.5	$0.779 \pm 0.007^{1,2,3}$	36.042 ± 0.198	13270.5	ND	ND	0.0	LMXB
106	4U 1730-335	$1.824 \pm 0.101^{1,2}$	3.294 ± 0.123	8863.1	1.784 ± 0.402^1	2.193 ± 0.298	4890.8	ND	ND	0.0	LMXB
107	SLX 1735-269	$0.360 \pm 0.030^{1,2,3}$	7.334 ± 0.095	13037.9	$0.490 \pm 0.081^{1,2,3}$	7.536 ± 0.180	13037.9	5.972 ± 3.115^3	2.667 ± 0.972	3757.6	LMXB
108	4U 1735-444	$0.329 \pm 0.014^{1,2,3}$	17.596 ± 0.213	6450.1	ND	ND	0.0	ND	ND	0.0	LMXB
109	IGR J17391-3021	$6.000 \pm 1.000^{1,2,3}$	0.821 ± 0.096	12685.8	$> 4.768^{1,3*}$	< 0.735	8667.8	ND	ND	0.0	HMXB
110	GRS 1736-297	3.057 ± 1.767^3	0.466 ± 0.183	3696.1	ND	ND	0.0	$> 8.061^{3*}$	< 1.469	3696.1	LMXB
111	XTE J1739-285	1.638 ± 0.164^2	2.463 ± 0.171	4085.8	1.695 ± 0.353^2	2.430 ± 0.331	4085.8	ND	ND	0.0	LMXB
112	IGR J17407-2808	1.908 ± 0.703^3	0.760 ± 0.181	3697.6	ND	ND	0.0	ND	ND	0.0	HMXB
113	SLX 1737-282	0.698 ± 0.105^3	2.444 ± 0.182	3713.8	ND	ND	0.0	ND	ND	0.0	LMXB
114	IGR J17419-2802	3.805 ± 1.813^2	0.507 ± 0.168	4118.9	ND	ND	0.0	ND	ND	0.0	UNID
115	XTE J1743-363	$1.346 \pm 0.151^{1,2}$	2.427 ± 0.138	8493.8	ND	ND	0.0	ND	ND	0.0	UNID
116	1E 1740.7-2942	$0.885 \pm 0.007^{1,2,3}$	18.157 ± 0.094	12625.5	$0.911 \pm 0.009^{1,2,3}$	26.844 ± 0.180	12625.5	$0.895 \pm 0.117^{1,2,3}$	17.816 ± 0.478	12625.5	LMXB
117	KS 1741-293	$1.184 \pm 0.072^{1,2}$	3.122 ± 0.110	8973.9	$1.402 \pm 0.170^{1,2}$	3.289 ± 0.209	8973.9	ND	ND	0.0	LMXB
118	GRS 1741.9-2853	$1.111 \pm 0.099^{2,3}$	2.542 ± 0.124	7708.5	2.413 ± 0.659^3	1.906 ± 0.357	3664.7	ND	ND	0.0	LMXB
119	IGR J17453-2853	0.841 ± 0.069^3	3.474 ± 0.181	3684.8	1.676 ± 0.422^3	2.183 ± 0.356	3684.8	ND	ND	0.0	LMXB
120	1A 1742-294	$0.787 \pm 0.014^{1,2,3}$	9.350 ± 0.095	12651.4	$1.240 \pm 0.069^{1,2,3}$	6.167 ± 0.181	12651.4	ND	ND	0.0	LMXB
121	IGR J17464-3213 ^g	$3.165 \pm 0.041^{1,2,3}$	10.883 ± 0.101	12428.2	$2.427 \pm 0.058^{1,2,3}$	11.404 ± 0.191	12428.2	$1.567 \pm 0.164^{1,3}$	11.485 ± 0.605	8521.1	LMXB
122	1A 1743-288	1.470 ± 0.104^2	3.445 ± 0.170	4088.0	1.675 ± 0.297^2	2.808 ± 0.331	4088.0	ND	ND	0.0	LMXB
123	IGR J17473-2721	5.072 ± 0.348^3	3.697 ± 0.179	3742.2	5.230 ± 0.632^3	4.121 ± 0.352	3742.2	ND	ND	0.0	LMXB
124	SLX 1744-299	$0.360 \pm 0.044^{1,2,3}$	6.000 ± 0.094	12718.3	$0.723 \pm 0.147^{1,2,3}$	4.641 ± 0.180	12718.3	ND	ND	0.0	LMXB
125	GX 3+1	$0.346 \pm 0.030^{1,2,3}$	7.503 ± 0.094	13168.1	ND	ND	0.0	ND	ND	0.0	LMXB
126	1A 1744-361	$> 7.992^{1*}$	< 0.278	4585.0	ND	ND	0.0	ND	ND	0.0	LMXB
127	AX J1749.1-2733	$2.186 \pm 0.418^{1,2}$	0.967 ± 0.110	9206.1	ND	ND	0.0	ND	ND	0.0	HMXB
128	GRO J1750-27	2.762 ± 0.064^3	10.984 ± 0.181	3774.3	2.688 ± 1.249^3	1.139 ± 0.356	3774.3	ND	ND	0.0	HMXB
129	IGR J17497-2821	2.877 ± 0.146^3	5.008 ± 0.180	3687.3	2.873 ± 0.177^3	8.093 ± 0.352	3687.3	2.580 ± 0.536^3	6.894 ± 0.961	3687.3	LMXB
130	SLX 1746-331	2.474 ± 0.684^1	0.891 ± 0.159	4824.6	2.045 ± 0.546^1	1.746 ± 0.293	4824.6	ND	ND	0.0	LMXB
131	SAX J1750.8-2900	3.084 ± 0.581^3	1.377 ± 0.183	3676.5	3.347 ± 1.345^3	1.283 ± 0.358	3676.5	ND	ND	0.0	LMXB
132	IGR J17507-2856	2.893 ± 0.778^3	0.972 ± 0.183	3655.3	ND	ND	0.0	ND	ND	0.0	UNID

Table 3. continued.

Nr.	Name	20-40 keV			40-100 keV			100-200 keV			Class
		V	F (10^{-11} ergs s^{-1} cm^{-2})	E (ksec)	V	F (10^{-11} ergs s^{-1} cm^{-2})	E (ksec)	V	F (10^{-11} ergs s^{-1} cm^{-2})	E (ksec)	
133	XTE J1751-305	> 6.395 ^{2*}	< 0.263	3990.4	ND	ND	0.0	ND	ND	0.0	LMXB
134	SWIFT J1753.5-0127	0.558 ± 0.004 ^{2,3}	43.636 ± 0.211	3001.7	0.587 ± 0.005 ^{2,3}	72.753 ± 0.450	3001.7	0.974 ± 0.052 ²	65.056 ± 2.346	1182.1	LMXB
135	IGR J17544-2619	5.379 ± 1.265 ^{1,2,3}	0.586 ± 0.095	13107.9	ND	ND	0.0	ND	ND	0.0	HMXB
136	IGR J17597-2201 ^g	0.608 ± 0.049 ¹	4.474 ± 0.162	5355.6	0.892 ± 0.105 ¹	5.040 ± 0.299	5355.6	ND	ND	0.0	LMXB
137	GX 5-1	0.585 ± 0.003 ^{1,2,3}	33.376 ± 0.097	13357.4	1.529 ± 0.305 ¹	2.415 ± 0.278	5134.8	ND	ND	0.0	LMXB
138	GRS 1758-258	0.333 ± 0.002 ^{1,2,3}	37.359 ± 0.097	13251.7	0.363 ± 0.003 ^{1,2,3}	60.096 ± 0.184	13251.7	0.430 ± 0.058 ^{1,2,3}	41.703 ± 0.488	13251.7	LMXB
139	GX 9+1	0.298 ± 0.025 ^{1,2,3}	10.890 ± 0.110	14186.3	ND	ND	0.0	ND	ND	0.0	LMXB
140	IGR J18027-2016	0.891 ± 0.097 ^{1,2,3}	3.316 ± 0.111	14175.0	2.797 ± 1.166 ³	1.447 ± 0.404	4427.4	ND	ND	0.0	HMXB
141	XTE J1807-294 ^g	3.492 ± 1.143 ¹	0.704 ± 0.157	4925.0	ND	ND	0.0	ND	ND	0.0	LMXB
142	SGR 1806-20	2.026 ± 0.219 ^{1,3}	1.984 ± 0.135	9837.6	1.677 ± 0.222 ¹	3.756 ± 0.328	5355.9	ND	ND	0.0	GRB
143	XTE J1810-189	2.825 ± 0.280 ³	3.095 ± 0.216	4586.4	2.980 ± 0.562 ³	3.244 ± 0.427	4586.4	ND	ND	0.0	HMXB
144	SAX J1810.8-2609	1.768 ± 0.089 ³	5.576 ± 0.197	3986.1	1.866 ± 0.173 ³	5.909 ± 0.380	3986.1	ND	ND	0.0	LMXB
145	GX 13+1	0.644 ± 0.037 ^{1,2,3}	7.601 ± 0.134	13306.4	ND	ND	0.0	ND	ND	0.0	LMXB
146	4U 1812-12	0.225 ± 0.016 ^{1,2,3}	18.049 ± 0.146	8364.3	0.265 ± 0.045 ^{1,2,3}	22.116 ± 0.293	8364.3	ND	ND	0.0	LMXB
147	GX 17+2	0.502 ± 0.003 ^{1,2,3}	39.952 ± 0.146	10505.6	ND	ND	0.0	ND	ND	0.0	LMXB
148	SWIFT J1816.7-1613	> 4.363 ^{2*,3}	< 0.653	8030.4	ND	ND	0.0	ND	ND	0.0	HMXB
149	IGR J18173-2509	2.470 ± 0.907 ¹	0.732 ± 0.174	5089.1	ND	ND	0.0	ND	ND	0.0	CV
150	XTE J1817-330	1.898 ± 0.060 ²	9.320 ± 0.209	3665.6	1.838 ± 0.119 ²	8.828 ± 0.401	3665.6	ND	ND	0.0	UNID
151	XTE J1818-245 ^g	3.495 ± 0.987 ^{2,3}	0.803 ± 0.150	8391.2	> 6.571 ^{2*}	< 0.584	4246.5	ND	ND	0.0	UNID
152	SAX J1818.6-1703	4.756 ± 0.815 ^{1,2,3}	1.161 ± 0.135	13305.8	4.957 ± 2.061 ^{1,3}	1.147 ± 0.308	9381.5	ND	ND	0.0	HMXB
153	AX J1820.5-1434	2.838 ± 0.743 ^{1,3}	1.072 ± 0.170	7942.9	ND	ND	0.0	ND	ND	0.0	HMXB
154	H 1820-303	0.317 ± 0.009 ^{1,2,3}	25.088 ± 0.124	12446.9	2.029 ± 0.416 ²	3.018 ± 0.407	3717.7	ND	ND	0.0	LMXB
155	H 1822-000	1.648 ± 0.518 ^{1,3}	1.163 ± 0.188	5190.6	ND	ND	0.0	ND	ND	0.0	LMXB
156	3A 1822-371	0.274 ± 0.013 ^{1,2,3}	21.952 ± 0.161	10735.5	ND	ND	0.0	ND	ND	0.0	LMXB
157	IGR J18259-0706	2.909 ± 1.485 ³	0.646 ± 0.227	2944.8	ND	ND	0.0	ND	ND	0.0	AGN
158	Ginga 1826-24	0.227 ± 0.002 ^{1,2,3}	58.774 ± 0.131	13300.6	0.241 ± 0.006 ^{1,2,3}	57.864 ± 0.245	13300.6	ND	ND	0.0	LMXB
159	IGR J18325-0756	1.419 ± 0.233 ^{1,2}	2.014 ± 0.189	4556.7	ND	ND	0.0	ND	ND	0.0	UNID
160	XB 1832-330	0.381 ± 0.049 ²	6.841 ± 0.259	3285.9	ND	ND	0.0	ND	ND	0.0	LMXB
161	Ser X-1	0.323 ± 0.049 ^{1,2,3}	7.551 ± 0.143	7700.9	ND	ND	0.0	ND	ND	0.0	LMXB
162	IGR J18406-0539	3.930 ± 1.616 ¹	0.881 ± 0.254	2746.4	> 5.663 ^{2*}	< 0.805	2321.6	ND	ND	0.0	HMXB
163	IGR J18410-0535	3.862 ± 1.187 ^{1,2}	0.860 ± 0.182	5097.1	> 4.837 ^{1,2*}	< 0.885	5097.1	ND	ND	0.0	HMXB
164	AX J1841.3-0455	ND	ND	0.0	1.360 ± 0.356 ²	3.408 ± 0.531	2398.7	4.763 ± 2.214 ²	4.626 ± 1.457	2398.7	HMXB
165	IGR J18450-0435	2.009 ± 0.576 ^{1,2,3}	1.080 ± 0.147	8550.2	ND	ND	0.0	ND	ND	0.0	HMXB
166	Ginga 1843+009	1.983 ± 0.193 ^{1,2,3}	2.215 ± 0.137	8557.6	> 2.347 ^{2,3*}	< 2.300	5584.1	ND	ND	0.0	HMXB
167	IGR J18483-0311	2.092 ± 0.155 ^{1,2,3}	2.936 ± 0.145	8745.6	2.019 ± 0.536 ^{1,2,3}	2.346 ± 0.290	8745.6	ND	ND	0.0	HMXB
168	3A 1850-087	0.606 ± 0.129 ^{1,3}	3.514 ± 0.201	5609.1	ND	ND	0.0	ND	ND	0.0	LMXB
169	IGR J18539+0727	> 3.774 ^{1,2*}	< 0.541	4659.1	4.301 ± 2.238 ¹	1.011 ± 0.365	2549.1	ND	ND	0.0	UNID
170	V1223 Sgr	0.531 ± 0.088 ³	5.267 ± 0.360	3038.9	ND	ND	0.0	ND	ND	0.0	CV
171	XTE J1855-026	0.915 ± 0.031 ^{1,2,3}	7.383 ± 0.145	8413.8	1.007 ± 0.184 ^{1,2,3}	5.454 ± 0.288	8413.8	ND	ND	0.0	HMXB
172	XTE J1858+034	2.488 ± 0.065 ^{1,2}	7.716 ± 0.142	5092.5	2.337 ± 0.882 ¹	1.435 ± 0.359	2739.9	ND	ND	0.0	HMXB
173	HETE J1900.1-2455	0.492 ± 0.013 ^{2,3}	19.234 ± 0.284	4331.0	0.578 ± 0.035 ^{2,3}	21.219 ± 0.566	4331.0	ND	ND	0.0	LMXB
174	4U 1901+03	1.090 ± 0.008 ¹	34.868 ± 0.187	2724.2	1.199 ± 0.144 ¹	4.586 ± 0.357	2724.2	ND	ND	0.0	HMXB
175	XTE J1908+094	ND	ND	0.0	2.471 ± 0.797 ¹	1.698 ± 0.362	2339.5	ND	ND	0.0	LMXB
176	H 1907+097	0.744 ± 0.054 ^{1,2,3}	10.273 ± 0.124	6332.8	ND	ND	0.0	ND	ND	0.0	HMXB

Table 3. continued.

Nr.	Name	20-40 keV			40-100 keV			100-200 keV			Class
		V	F (10^{-11} ergs s^{-1} cm^{-2})	E (ksec)	V	F (10^{-11} ergs s^{-1} cm^{-2})	E (ksec)	V	F (10^{-11} ergs s^{-1} cm^{-2})	E (ksec)	
177	4U 1909+07	$0.594 \pm 0.016^{1,2,3}$	9.089 ± 0.121	6595.4	$0.607 \pm 0.137^{1,2,3}$	6.522 ± 0.242	6595.4	ND	ND	0.0	HMXB
178	IGR J19112+1358	$> 4.516^{3*}$	< 0.379	2251.2	ND	ND	0.0	ND	ND	0.0	UNID
179	Aql X-1	$1.928 \pm 0.048^{1,2,3}$	7.825 ± 0.137	7327.5	$1.927 \pm 0.095^{1,2,3}$	8.334 ± 0.272	7327.5	ND	ND	0.0	LMXB
180	SS 433	$0.729 \pm 0.033^{1,2,3}$	5.876 ± 0.123	6809.4	0.866 ± 0.171^3	4.911 ± 0.528	2102.8	ND	ND	0.0	HMXB
181	IGR J19140+0951	$1.630 \pm 0.082^{1,2,3}$	6.169 ± 0.124	6314.8	$1.734 \pm 0.178^{1,2,3}$	4.446 ± 0.249	6314.8	ND	ND	0.0	HMXB
182	GRS 1915+105	$0.506 \pm 0.001^{1,2,3}$	182.501 ± 0.128	6278.2	$0.568 \pm 0.002^{1,2,3}$	100.967 ± 0.256	6278.2	$0.686 \pm 0.065^{2,3}$	34.835 ± 0.945	4015.8	LMXB
183	4U 1916-053	$0.391 \pm 0.083^{1,2}$	5.909 ± 0.221	3788.5	ND	ND	0.0	ND	ND	0.0	LMXB
184	KS 1947+300	$1.317 \pm 0.091^{1,2}$	8.906 ± 0.424	1376.9	$1.201 \pm 0.221^{1,2}$	7.845 ± 0.809	1376.9	ND	ND	0.0	HMXB
185	3A 1954+319	$1.018 \pm 0.035^{2,3}$	12.188 ± 0.287	2146.0	0.774 ± 0.128^3	7.215 ± 0.692	1498.8	ND	ND	0.0	LMXB
186	Cyg X-1	$> 0.265^{1,2,3}$	< 505.064	3255.1	$> 0.289^{1,2,3}$	< 742.342	3255.1	$0.327 \pm 0.002^{1,2,3}$	505.242 ± 1.283	3255.1	HMXB
187	EXO 2030+375	$2.218 \pm 0.017^{1,2,3}$	36.696 ± 0.203	3116.2	$2.122 \pm 0.050^{1,2,3}$	24.136 ± 0.399	3116.2	$> 5.735^{3*}$	< 3.575	1092.4	HMXB
188	Cyg X-3	$0.357 \pm 0.001^{1,2,3}$	110.404 ± 0.197	3130.7	$0.338 \pm 0.005^{1,2,3}$	56.916 ± 0.390	3130.7	ND	ND	0.0	HMXB
189	SAX J2103.5+4545	$1.497 \pm 0.045^{1,3}$	9.366 ± 0.198	2927.3	$1.617 \pm 0.150^{1,3}$	6.412 ± 0.406	2927.3	ND	ND	0.0	HMXB
190	IGR J21247+5058	0.270 ± 0.039^3	5.227 ± 0.242	1564.6	ND	ND	0.0	ND	ND	0.0	AGN
191	4U 2129+12	ND	ND	0.0	1.313 ± 0.806^2	3.870 ± 1.645	133.0	ND	ND	0.0	LMXB
192	SS Cyg	1.005 ± 0.205^1	2.413 ± 0.317	1147.2	ND	ND	0.0	ND	ND	0.0	CV
193	Cyg X-2	$0.421 \pm 0.017^{1,2,3}$	17.769 ± 0.265	2793.1	ND	ND	0.0	ND	ND	0.0	LMXB
194	3A 2206+543	$1.043 \pm 0.071^{1,2,3}$	5.679 ± 0.224	2923.0	$0.946 \pm 0.276^{1,2,3}$	5.365 ± 0.485	2923.0	ND	ND	0.0	HMXB
195	3C 454.3	0.369 ± 0.063^2	6.229 ± 0.572	271.3	ND	ND	0.0	ND	ND	0.0	AGN
196	<i>gam Cas</i>	0.358 ± 0.138	2.981 ± 0.177	2741.3	ND	ND	0.0	ND	ND	0.0	HMXB
197	<i>RX J0137.7+5814</i>	$> 4.075^{1*}$	< 0.349	2477.1	ND	ND	0.0	ND	ND	0.0	UNID
198	<i>Vela Pulsar</i>	0.207 ± 0.080	4.560 ± 0.152	2955.5	ND	ND	0.0	ND	ND	0.0	SNR
199	<i>IGR J08408-4503</i>	$> 3.937^{1*}$	< 0.225	2945.0	ND	ND	0.0	ND	ND	0.0	HMXB
200	<i>NGC 4051</i>	1.113 ± 0.548	1.249 ± 0.265	1483.4	ND	ND	0.0	ND	ND	0.0	AGN
201	<i>PKS 1241-399</i>	$> 3.411^{1*}$	< 0.530	1312.7	ND	ND	0.0	ND	ND	0.0	AGN
202	<i>SWIFT J1922.7-1716</i>	3.266 ± 2.396	0.640 ± 0.269	2804.3	ND	ND	0.0	ND	ND	0.0	UNID

The table gives the values of fractional variability of the sources, V_r , and the flux, F , in 10^{-11} ergs s^{-1} cm^{-2} and corresponding 2σ errors. The conversion factors⁷ are $1 \text{ c/s} = 4.46 \times 10^{-11}$ ergs s^{-1} cm^{-2} (20-40 keV), $1 \text{ c/s} = 9.247 \times 10^{-11}$ ergs s^{-1} cm^{-2} (40-100 keV), and $1 \text{ c/s} = 3.638 \times 10^{-10}$ ergs s^{-1} cm^{-2} (100-200 keV). The exposure time of the sources, E , in ksec is given for each energy band only if the source was detected. The class column gives the source type according to the reference catalog. If the source is localized in more than one map then the weighted mean values of the flux and variability are given. The sources active during specific time periods and not detected at the total variability map are indicated with bold font. The sources detected only on the total variability map are indicated with italics. The superscript numbers show the time period map where the source is visible and asterisk means that the source is not detected at the respective significance map. Lower limit for fractional variability is given in such a case. The superscript “g” indicates that the source was affected by the “ghost”.

⁷ We used the OSA 7.0 ARFs and RMFs and simulated a source with a Crab-like spectrum. Then using XSPEC we found the conversion between count rate and flux. It should be noted that this method depends on the spectral shape of the source, and that there are several ARFs for different periods of the mission, so the fluxes cannot be fully reliable. However, we find this approach the most suitable for the current catalog paper.